Anisotropic nonlocal damage model for materials with intrinsic transverse isotropy

Wencheng Jin[a], Chloé Arson[a,*]

[a]*School of Civil and Environmental Engineering, Georgia Institute of Technology, USA*

Abstract

This paper presents the theoretical formulation and numerical implementation of an anisotropic damage model for materials with intrinsic transverse isotropy. Crack initiation and propagation are modeled by phenomenological damage evolution laws, controlled by four equivalent strain measures. The latter are constructed so as to distinguish the mechanical response of the material in tension and compression, along the direction perpendicular to the bedding plane and within the bedding plane. To avoid mesh dependency induced by softening, equivalent strains are replaced by nonlocal counterparts, defined as weighted averages over a neighborhood scaled by two internal length parameters. Finite Element equations are solved with a normal plane arc length control algorithm, which allows passing limit points in case of snap back or snap through. The model is calibrated against triaxial compression tests performed on shale, for different confinements and loading orientations relative to the bedding plane. Gauss point simulations confirm that the model successfully captures the variation of uniaxial tensile strength with respect to the bedding orientation. Finite Element simula-

---

*Corresponding author
 Email address: chloe.arson@ce.gatech.edu (Chloé Arson)

tions of three-point bending tests and compression splitting tests show that nonlocal enhancement indeed avoids mesh dependency, and that the axial and transverse dimensions of the damage process zone are scaled by the two characteristic lengths. Results further show that the damage process zone is direction dependent both in tension and compression. The model can be used for any type of textured brittle material; it allows representing several concurrent damage mechanisms in the macroscopic response and interpreting the failure mechanisms that control the damage process zone.

1. Introduction

Many geomaterials exhibit strong orientation dependent mechanical behavior (anisotropy) due to bedding, layering or crack patterns, as evidenced in shale (Niandou et al., 1997; Gautam and Wong, 2006; Sone and Zoback, 2013), clay stone (OKA et al., 2002), schists (Nasseri et al., 2003) and sand (Dafalias et al., 2004). Laboratory tests, such as uniaxial and triaxial compression tests (Niandou et al., 1997; Nasseri et al., 2003; Fu et al., 2012), Brazilian indirect tension tests (Cho et al., 2012; Vervoort et al., 2014), direct shear tests (Heng et al., 2015) and triaxial shear tests (Ye and Ghassemi, 2016), further demonstrate that material strength and failure modes significantly depend on the confining pressure and the loading orientation with respect to microstructure. Prior to crack propagation, most geomaterials can be considered transverse isotropic: the maximum uniaxial compressive

strength is reached when weak planes are either parallel or perpendicular to the loading direction, and the minimum strength is reached when weak planes are oriented at $30° − 60°$ with respect to the loading direction (Donath, 1961; Niandou et al., 1997). In indirect tensile tests, the tensile strength is maximum when tensile stress is applied within the weak plane, and gradually decreases as the orientation angle between the tensile stress direction and the bedding plane increases (Cho et al., 2012).

In geomaterials models, intrinsic and induced anisotropy are either accounted for in the failure criterion or in the expression of the free energy. Hill (1948) extended the von Mises yield criterion to orthotropic ductile materials, by using 6 quadratic stress terms. To further account for the strength difference in tension and compression, Hoffman (1967) added 3 linear terms of stress into Hill's failure criterion. Tsai and Wu (1971) then expressed failure criteria that depend on all possible linear and quadratic stress terms. These yield criteria were used by de Borst (Schellekens and De Borst, 1990; Hashagen and De Borst, 2001) to model perfectly plastic and hardening materials. Reinicke and Ralston (1977) carried out limit analyses using parabolic yield functions (Hoffman's criteria).

Other approaches were proposed to introduce either the fourth order projection tensor or the second order microstructure tensor in the yield criteria or in the expression of the free energy. Boehler and Sawczuk (1977) used the microstructure tensor in the constitutive model for transverse isotropic materials. Cazacu et al. (1998), Cazacu and Cristescu (1999) employed a fourth order projection tensor to transform the stress tensor into a characteristic tensor with embedded microstructure information. They extended

the Mises-Schleicher yield criterion initially expressed for isotropic materials to transversely isotropic materials, by using the fourth order characteristic tensor. Another approach, based on different projection tensors, consists in projecting the strength in Drucker-Prager and Mohr-Coulomb yield criteria (Rouabhi et al., 2007). The microstructure tensor can also be constructed with eigenvectors representing the axes of material symmetry to capture the orientation dependence of strain hardening, softening, damage and plasticity in shale (Pietruszczak and Mroz, 2000, 2001; Pietruszczak et al., 2002; Chen et al., 2010). For soils, fabric tensors were used to represent microstructure in yield criteria (Oda and Nakayama, 1989). Thermodynamic models were also proposed, in which the free energy was expressed in terms of microstructure tensor and strain invariants (Halm et al., 2002; Nedjar, 2016).

Alternatively, the Representative Element Volume (REV) can be viewed as a set of cracks or planes of discontinuities. Intrinsic anisotropy is accounted for by assigning different material properties to crack families of different orientations (Chen et al., 2012; Hu et al., 2013). In micromechanics models, a static constraint is applied to projections of stress on the crack planes, and the expression of the REV free energy is obtained by homogenization. In microplane models, a kinematic constraint is applied to projections of strains on the crack planes; the principle of virtual work is used to upscale the microscopic relationships and calculate the macroscopic stress. Anisotropy is accounted for by considering complex microplane orientation distributions and by formulating different evolution criteria for different microplanes (Li et al., 2017).

Once implemented in the Finite Element Method (FEM), anisotropic

models that account for plastic/damage softening suffer from mesh dependency. Integration-based nonlocal formulations alleviate spurious mesh sensitivity but cannot be easily used with stress-based yield/damage criteria, in which the out-of-balance stress at a point has to be calculated iteratively from the yet-unknown stress in a given neighborhood. Hence in this paper, we integrate a measure of strain to formulate a nonlocal anisotropic damage model for transverse isotropic geomaterials. In Section 2, we formulate a constitutive law for predicting stress-induced anisotropy in an initially transverse isotropic material. The evolution laws of damage components are expressed in terms of equivalent strains, which are direction dependent. Two internal length parameters are used to avoid mesh dependency and account for intrinsic anisotropy. In Section 3, we calibrate the model against stress/strain curves obtained during triaxial compression tests performed on shale. A sensitivity analysis is presented based on a series of uniaxial tension tests simulated on a single element (at the Gauss point). In Section 4, we present simulations of three-point bending and splitting tests and we show that the size of the fracture process zone is direction dependent, but mesh independent. Results also reveal the underlying failure mechanisms associated to damage orientation. Note that we use Voigt matrix notations throughout the paper. Lower cases are used for scalar variables, bold lower cases for vectors and bold upper cases for matrices. Note that the soil mechanics sign convention is adopted throughout the paper, in which compression is counted positive.

2. Formulation and Implementation of the Nonlocal Anisotropic Damage Model for Transverse Isotropic Materials

2.1. Damage operator and damaged stiffness tensor

At the scale of the REV, the inception, propagation and coalescence of micro-cracks result in hardening or softening of stress/strain relations and stiffness reduction. The nominal stress, $\boldsymbol{\sigma}$, is related to the damaged effective stress, $\hat{\boldsymbol{\sigma}}$, through

$$\hat{\boldsymbol{\sigma}} = \mathbf{M}\boldsymbol{\sigma} \tag{1}$$

Where $\mathbf{M}$ is a damage operator. Assuming that damage components in each direction evolve independently, the damage operator $\mathbf{M}$ has a diagonal form, as follows:

$$M_{ii} = \frac{1}{1 - \omega_i} \quad i = 1, 2, ..., 6 \tag{2}$$

Note that Voigt notations are adopted here, so that $\hat{\sigma}_4 = \hat{\tau}_{23} = \frac{\tau_{23}}{1-\omega_4}$, in which:

$$
\begin{aligned}
\omega_4 &= 1 - (1 - \omega_2)(1 - \omega_3) \\
\omega_5 &= 1 - (1 - \omega_1)(1 - \omega_3) \\
\omega_6 &= 1 - (1 - \omega_1)(1 - \omega_2)
\end{aligned}
\tag{3}
$$

The diagonal form of $\mathbf{M}$ ensures that the damaged compliance matrix resulting from equation 1 is symmetrical. We consider a geomaterial with transverse isotropy with respect to the normal direction of bedding planes. Fig.1 shows the example of shale, which is a sedimentary rock (Gautam and Wong, 2006; Waters et al., 2011; Ye et al., 2016). We set the local coordinate system so that direction 1, called the axial direction, is perpendicular to the bedding plane. Directions 2 and 3, along the bedding plane, are called
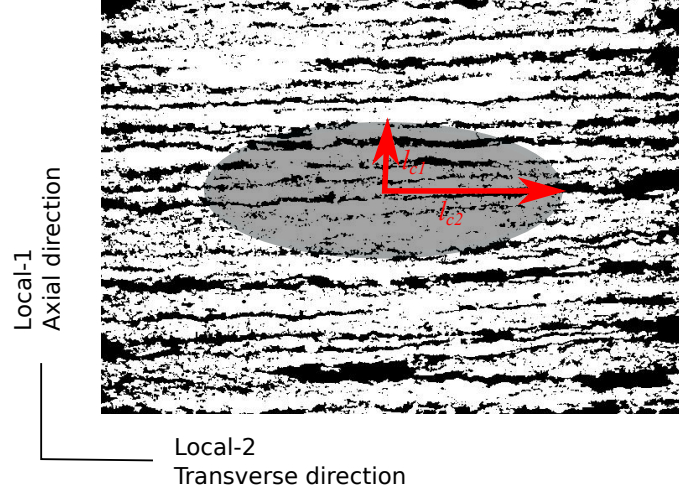
Figure 1: Definition of the intrinsic damage directions in transverse isotropic shale, modified from Bramlette (1943).

transverse directions. Correspondingly, in Eq.2, ω_1 is called axial damage and ω_2, ω_3 are the transverse damage variables.

We focus on transverse isotropic behavior in quasi-brittle materials. With negligible inelastic deformation, the non-linear stress/strain behavior results from damage evolution only (micro-crack development). Adopting the principle of strain equivalence, the constitutive relation is expressed as

$$\boldsymbol{\epsilon} = \mathbf{S}^0 \mathbf{M} \boldsymbol{\sigma}. \tag{4}$$

For a transverse isotropic material, the elastic compliance matrix $\mathbf{S}^0$ depends

on 5 parameters. In the local coordinate system, $\mathbf{S}^0$ is expressed as:

$$\mathbf{S}^0 = \begin{pmatrix} \frac{1}{E_1} & -\frac{\nu_{12}}{E_2} & -\frac{\nu_{12}}{E_2} & 0 & 0 & 0 \\ -\frac{\nu_{21}}{E_1} & \frac{1}{E_2} & -\frac{\nu_{23}}{E_2} & 0 & 0 & 0 \\ -\frac{\nu_{21}}{E_1} & -\frac{\nu_{32}}{E_2} & \frac{1}{E_2} & 0 & 0 & 0 \\ 0 & 0 & 0 & \frac{2(1+\nu_{23})}{E_2} & 0 & 0 \\ 0 & 0 & 0 & 0 & \frac{1}{G_{13}} & 0 \\ 0 & 0 & 0 & 0 & 0 & \frac{1}{G_{12}} \end{pmatrix} \tag{5}$$

Where $\frac{\nu_{12}}{E_2} = \frac{\nu_{21}}{E_1}, \nu_{23} = \nu_{32}$ and $G_{13} = G_{12}$.

We construct damage evolution laws that directly relate damage components to equivalent strain measures, defined below. We focus on plane strain loading conditions, in which the out-of-plane components of equivalent strains are zero, and consequently, the out-of-plane component of damage, ω_3, is zero. With $\omega_3 = 0$, the damaged stiffness matrix $\mathbf{C}$ can be explicitly expressed as

$$\mathbf{C} = \begin{pmatrix} C_{11} & C_{12} & C_{13} & 0 \\ C_{21} & C_{22} & C_{23} & 0 \\ C_{31} & C_{32} & C_{33} & 0 \\ 0 & 0 & 0 & C_{44} \end{pmatrix} \tag{6}$$

8

in which

$$C_{11} = E_1(1-\omega_1)((1-\omega_2)\nu_{23}^2 - 1)/D$$

$$C_{22} = E_2(1-\omega_2)((1-\omega_1)\nu_{12}\nu_{21} - 1)/D$$

$$C_{33} = E_2(1-\omega_1)(1-\omega_2)(\nu_{21}\nu_{12} - 1)/D$$

$$C_{44} = G_{12}(1-\omega_1)(1-\omega_2)$$

$$C_{12} = -E_1\nu_{21}(1-\omega_1)(1-\omega_2)(1+\nu_{23})/D \qquad (7)$$

$$C_{21} = -E_2\nu_{12}(1-\omega_1)(1-\omega_2)(1+\nu_{23})/D$$

$$C_{13} = -E_1\nu_{21}(1-\omega_1)(1+(1-\omega_2)\nu_{23})/D$$

$$C_{31} = -E_2\nu_{12}(1-\omega_1)(1+(1-\omega_2)\nu_{23})/D$$

$$C_{32} = C_{23} = -E_2(1-\omega_2)(\nu_{23}+(1-\omega_1)\nu_{12}\nu_{21})/D$$

Where $\boldsymbol{\sigma} = \mathbf{C} : \boldsymbol{\epsilon}$, $E_2\nu_{12} = E_1\nu_{21}$, and

$$D = (1-\omega_2)\nu_{23}^2 + 2(1-\omega_1)(1-\omega_2)\nu_{12}\nu_{21}\nu_{23} + (1-\omega_1)(2-\omega_2)\nu_{12}\nu_{21} - 1$$
$$(8)$$

2.2. Concept of equivalent strain

Equivalent strains can take various forms (Huerta and Pijaudier-Cabot, 1994; Mazars, 1986; De Vree et al., 1995; Desmorat et al., 2007; Comi and Perego, 2004; Jirásek and Patzák, 2002). For isotropic materials, the most widely used equivalent strains are: the energy release rate thermodynamically conjugated to damage (Huerta and Pijaudier-Cabot, 1994), the square root of the positive principal strains (Mazars, 1986), and a modified von Mises strain (De Vree et al., 1995). Equivalent strain measures were introduced in damage evolution laws to capture unilateral effects, differences of behavior in tension and compression, and macroscopic hardening and softening due to

9

mixed mode micro crack initiation and propagation. For direction dependent transverse isotropic materials, a complete set of new equivalent strains needs to be defined. Inspired from the stress invariants used in Hill's yield criterion (Hill, 1948) and in Hashin's failure criterion (Hashin, 1980) (for unidirectional fiber composites), we introduce the following strain measures, which are strain invariants if axis 1 is normal to the bedding planes:

$$
\begin{aligned}
I_1 &= \epsilon_{11} \\
I_2 &= \epsilon_{22} + \epsilon_{33} \\
I_3 &= \frac{1}{4}(\epsilon_{22} - \epsilon_{33})^2 + \epsilon_{23}^2 \\
I_4 &= \epsilon_{12}^2 + \epsilon_{13}^2 \\
I_5 &= 2\epsilon_{12}\epsilon_{13}\epsilon_{23} - \epsilon_{22}\epsilon_{13}^2 - \epsilon_{33}\epsilon_{12}^2
\end{aligned}
\tag{9}
$$

I_3 is the square of the maximum transverse shear strain while I_4 is the square of the maximum axial shear strain. Following the form of Hill's and Hashin's models, we choose a quadratic damage criterion. Based on the invariants defined above, the most general form of a transversely isotropic *quadratic* failure criterion is

$$
A_1 I_1^2 + A_2 I_2^2 + A_3 I_3 + A_4 I_4 + B_{12} I_1 I_2 = 1
\tag{10}
$$

In which A_1, A_2, A_3, A_4 and B_{12} are material parameters. Field investigation and laboratory experiments (Tien and Kuo, 2001; Gallant et al., 2007) indicate that there are two primary failure modes in transversely isotropic rock (Fig.2): the sliding mode, in which failure is controlled by the shear strength of the bedding planes, and the non-sliding mode, in which failure is controlled by the strength of the matrix material. In sliding mode, failure is the result of normal and shear stresses, and occurs along the bedding
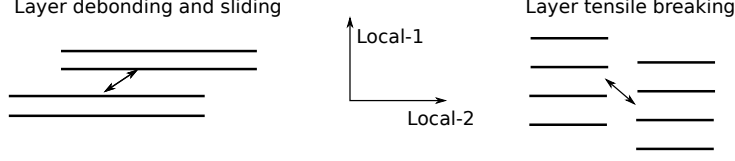
Figure 2: The two primary failure modes in transversely isotropic materials.

plane $(x_2 - x_3)$. In terms of continuum mechanics variables, it implies that failure in sliding mode is controlled by strain components $\epsilon_{11}, \epsilon_{12}$ and ϵ_{13}. In non-sliding mode, the normal direction of the failure surface is contained in the bedding plane. Due to material isotropy in the bedding plane $(x_2 - x_3)$, failure in non-sliding mode is controlled by all strain components except ϵ_{11}. Consequently, we are seeking two failure criteria expressed in the following form:

$$
\begin{aligned}
A_1 I_1^2 + A_4 I_4 &= 1 \\
A_2 I_2^2 + A_3 I_3 + A_4 I_4 &= 1
\end{aligned}
\tag{11}
$$

for the sliding mode and the non-sliding mode, respectively.

We define the equivalent strain measures as $\epsilon_1^{eq}/\kappa_1^0 = \sqrt{A_1 I_1^2 + A_4 I_4}$ and $\epsilon_2^{eq}/\kappa_2^0 = \sqrt{A_2 I_2^2 + A_3 I_3 + A_4 I_4}$. Noting ϵ_{11}^{t0} (respectively ϵ_{22}^{t0}) and ϵ_{11}^{c0} (respectively ϵ_{22}^{c0}) the initial tensile and compressive strain thresholds for the sliding mode (respectively for the non-sliding mode), we have $\kappa_1^0 = \epsilon_{11}^{t0}$ (respectively $\kappa_2^0 = \epsilon_{22}^{t0}$) in tension, $\kappa_1^0 = \epsilon_{11}^{c0}$ (respectively $\kappa_2^0 = \epsilon_{22}^{c0}$) in compression. Hence the equivalent strain in the axial direction is constructed as:

$$
\epsilon_{1j}^{eq} = \sqrt{I_1^2 + I_4 \left(\epsilon_{11}^{j0}/\epsilon_{12}^{s0}\right)^2} = \sqrt{(\epsilon_{11})^2 + ((\epsilon_{12})^2 + (\epsilon_{13})^2) \left(\frac{\epsilon_{11}^{j0}}{\epsilon_{12}^{s0}}\right)^2}, \quad j = t, c
\tag{12}
$$

We took $A_1^j = 1/(\epsilon_{11}^{j0})^2$ and $A_4 = 1/(\epsilon_{12}^{s0})^2$ where ϵ_{12}^{s0} is the initial out-of-

bedding-plane shear strain threshold. Similarly, the equivalent strain in the transverse directions is defined as:

$$
\epsilon_{2j}^{eq} = \sqrt{I_2^2 + I_3 \left(\frac{\epsilon_{22}^{j0}}{\epsilon_{23}^{s0}}\right)^2 + I_4 \left(\frac{\epsilon_{22}^{j0}}{\epsilon_{12}^{s0}}\right)^2}, \quad j = t,\, c
$$

$$
\epsilon_{2j}^{eq} = \sqrt{(\epsilon_{22} + \epsilon_{33})^2 + \frac{1}{4}\left(\frac{\epsilon_{22}^{j0}}{\epsilon_{23}^{s0}}\right)^2 [(\epsilon_{22} - \epsilon_{33})^2 + \epsilon_{23}^2] + \left(\frac{\epsilon_{22}^{j0}}{\epsilon_{12}^{s0}}\right)^2 (\epsilon_{12}^2 + \epsilon_{13}^2)}
$$

(13)

We took $A_2^j = 1/(\epsilon_{22}^{j0})^2$ and $A_3 = 1/(\epsilon_{23}^{s0})^2$, where ϵ_{23}^{s0} is the initial shear strain threshold within the bedding plane.

2.3. Damage criteria and evolution laws in tension

Since crack orientations and propagation modes are different in tension and compression (Jin and Arson, 2017a,b), we distinguish tensile and compressive damage components, noted $\omega_{it}, \omega_{ic}, i = 1, 2, 3$ respectively. Unlike Mazars and Pijaudier-Cabot (1989), in which total damage is calculated as the weighted average of tensile and compressive damage components, we consider that tensile damage components ω_{it} and compressive damage components ω_{ic} are two sets of independent internal state variables. When the volumetric strain $\epsilon_v = \epsilon_1 + \epsilon_2 + \epsilon_3$ is positive (respectively, negative), compressive damage components ω_{ic} (respectively, tensile damage components ω_{it}) are substituted into Eq.2 to construct the damage operator. As a result, unilateral effects due to crack closure can be captured. Damage components take values between 0 (no micro-crack in the direction considered) and 1 (no more stiffness in the direction considered).

Two loading surfaces are used to distinguish micro-crack propagation in the axial and transverse directions. For tensile damage, we consider the two following damage criteria:

$$g_{1t}(\boldsymbol{\epsilon}, \kappa_1) = \epsilon_{1t}^{eq} - \kappa_1, \quad g_{2t}(\boldsymbol{\epsilon}, \kappa_2) = \epsilon_{2c}^{eq} - \kappa_2 \tag{14}$$

Where the equivalent strains ϵ_i^{eq} are scalar measures of strain defined in the axial and transverse directions. κ_1 and κ_2 are the internal variables that control the evolution of damage: they represent the equivalent strain thresholds before the initiation of damage in directions 1 and 2, respectively. After damage initiation, κ_1 and κ_2 are the largest equivalent strains ever reached during the past loading history of the material. Damage can only grow if the current stress state reaches the boundary of the elastic domain, $g_i = 0$. Karush-Kuhn-Tucker complementary conditions are used to account for loading-unloading stress paths:

$$
\begin{aligned}
g_1 \leq 0, \quad \dot{\kappa}_1 \geq 0, \quad \dot{\kappa}_1 g_1 = 0 \\
g_2 \leq 0, \quad \dot{\kappa}_2 \geq 0, \quad \dot{\kappa}_2 g_2 = 0
\end{aligned} \tag{15}
$$

Now, we establish a relationship between the internal variables κ_1, κ_2, defined as the maximum equivalent strains ever encountered in the material, and the damage variable $\boldsymbol{\omega}$. Since both the internal variables and the damage components grow monotonically, it is admissible to postulate the evolution law of damage in the form $\omega_i = f(\kappa_i)$, $i = 1, 2$. The exact form of the function f should be identified from actual stress paths monitored in experiments, such as uniaxial stress-strain curve in axial and transverse directions. In the absence of such data, we assume that in tension, the axial damage component follows an exponential law, which reflects rapid micro crack propagation in

13

mixed I-II mode:

$$\omega_{1t} = \begin{cases} 0, & \text{if } \kappa_1 \leq \epsilon_{11}^{t0} \\ 1 - \exp\left(-\frac{\kappa_1 - \epsilon_{11}^{t0}}{\alpha_{11}^{t}}\right), & \text{if } \kappa_1 > \epsilon_{11}^{t0} \end{cases} \tag{16}$$

Where α_{11}^{t} is a material parameter that controls the damage growth rate. We use a similar evolution law for tensile damage growth in the transverse directions:

$$\lambda_{2t} = \frac{1}{2}\left(\chi_{2t} + \chi_{3t}\right) = \begin{cases} 0, & \text{if } \kappa_2 \leq \epsilon_{22}^{t0} \\ 1 - \exp\left(-\frac{\kappa_2 - \epsilon_{22}^{t0}}{\alpha_{22}^{t}}\right), & \text{if } \kappa_2 > \epsilon_{22}^{t0} \end{cases} \tag{17}$$

Where α_{22}^{t} controls the ductility of the response in the transverse directions. Based on the definition of the equivalent strain ϵ_{2t}^{eq}, we split the transverse damage components as follows:

$$\chi_{2t} = 2\lambda_{2t} \frac{\epsilon_{22}^2 + \epsilon_{22}\epsilon_{33} + \left(\frac{1}{4}\langle\epsilon_{22} - \epsilon_{33}\rangle^2 + \frac{1}{2}(\epsilon_{23})^2\right)\left(\frac{\epsilon_{22}^{t0}}{\epsilon_{23}^{s0}}\right)^2 + \epsilon_{12}^2\left(\frac{\epsilon_{22}^{t0}}{\epsilon_{12}^{s0}}\right)^2}{(\kappa_2)^2}$$

$$\chi_{3t} = 2\lambda_{2t} \frac{\epsilon_{33}^2 + \epsilon_{22}\epsilon_{33} + \left(\frac{1}{4}\langle\epsilon_{33} - \epsilon_{22}\rangle^2 + \frac{1}{2}(\epsilon_{23})^2\right)\left(\frac{\epsilon_{22}^{t0}}{\epsilon_{23}^{s0}}\right)^2 + \epsilon_{13}^2\left(\frac{\epsilon_{22}^{t0}}{\epsilon_{12}^{s0}}\right)^2}{(\kappa_2)^2} \tag{18}$$

$$\omega_{2t} = \begin{cases} \bar{\omega}_{2t}, & \text{if } \chi_{2t} \leq \bar{\omega}_{2t} \\ \chi_{2t}, & \text{if } \chi_{2t} > \bar{\omega}_{2t} \end{cases}, \quad \omega_{3t} = \begin{cases} \bar{\omega}_{3t}, & \text{if } \chi_{3t} \leq \bar{\omega}_{3t} \\ \chi_{3t}, & \text{if } \chi_{3t} > \bar{\omega}_{3t} \end{cases}$$

Where we introduced the McAuley brackets: $\langle x \rangle = 0$ if $x < 0$, $\langle x \rangle = x$ if $x \geq 0$. $\bar{\omega}_{2t}$ and $\bar{\omega}_{3t}$ are the tensile damage values in the two transverse directions at the previous increment. Fig.3(a) below shows the evolution of tensile damage with the tensile equivalent strain: once the threshold is reached, damage evolves rapidly, and the growth rate slows down close to final failure.

14

2.4. Damage criteria and evolution laws in compression

Different from mixed mode crack propagation, pure mode II sliding in compression is confining (normal) stress dependent. We reconstruct the two compressive loading surfaces in axial and transverse directions as:

$$g_{1c}(\boldsymbol{\epsilon}, \kappa_1) = \epsilon_{1c}^{eq} + \eta \langle (\sigma_2 + \sigma_3)/2 \rangle - \kappa_1$$
$$g_{2c}(\boldsymbol{\epsilon}, \kappa_2) = \epsilon_{2c}^{eq} + \eta \langle \sigma_1 \rangle - \kappa_2 \tag{19}$$

Where η controls the influence of the confining stress on compressive damage. Note that the McAuley brackets are introduced to account for compressive confining stress only. Similar to tensile loading functions in Eq.14, the internal state variables κ_1, κ_2 in Eq.19 represent the largest value taken by the terms $\epsilon_{1c}^{eq} + \eta \langle (\sigma_2 + \sigma_3)/2 \rangle$, $\epsilon_{2c}^{eq} + \eta \langle \sigma_1 \rangle$ in the entire loading history of the material. Since geomaterials exhibit a pre-peak hardening and post-peak softening behavior for mode II sliding in compression (Amendt et al., 2013), we choose an evolution function $f(\kappa_1)$ with a low growth rate at the beginning and a high growth rate after the peak, as follows:

$$\omega_{1c} = \begin{cases} 0, & \text{if } \kappa_1 \leq \epsilon_{11}^{c0} \\ \dfrac{\exp\left[(\kappa_1 - \beta_{11}^c)/\alpha_{11}^c\right]}{1 + \exp\left[(\kappa_1 - \beta_{11}^c)/\alpha_{11}^c\right]}, & \text{if } \kappa_1 > \epsilon_{11}^{c0} \end{cases} \tag{20}$$

Where β_{11}^c and α_{11}^c are parameters that represent the initiation of softening in the absence of confinement and the damage growth rate in the axial direction, respectively. Fig.3(b) shows the evolution of compressive damage with the compressive equivalent strain. We define the evolution function $f(\kappa_2)$ in the transverse directions in a similar way as in the axial direction, as follows:

$$\lambda_{2c} = \frac{1}{2}\left(\chi_{2c} + \chi_{3c}\right) = \begin{cases} 0, & \text{if } \kappa_2 \leq \epsilon_{22}^{c0} \\ \dfrac{\exp\left[(\kappa_2 - \beta_{22}^c)/\alpha_{22}^c\right]}{1 + \exp\left[(\kappa_2 - \beta_{22}^c)/\alpha_{22}^c\right]}, & \text{if } \kappa_2 > \epsilon_{22}^{c0} \end{cases} \tag{21}$$

15

In which we split the transverse damage components based on the definition of equivalent strain ϵ_{2c}^{eq} in Eq.13 and loading surface in Eq.19, as follows:

$$\chi_{2c} = 2\lambda_{2c} \frac{\epsilon_{22}^2 + \epsilon_{22}\epsilon_{33} + \left(\frac{1}{4}\langle\epsilon_{22} - \epsilon_{33}\rangle^2 + \frac{1}{2}(\epsilon_{23})^2\right)\left(\frac{\epsilon_{22}^{c0}}{\epsilon_{23}^{s0}}\right)^2 + \epsilon_{12}^2\left(\frac{\epsilon_{22}^{c0}}{\epsilon_{12}^{s0}}\right)^2 + \frac{\eta\langle\sigma_1\rangle}{2}}{(\kappa_2)^2}$$

$$\chi_{3c} = 2\lambda_{2c} \frac{\epsilon_{33}^2 + \epsilon_{22}\epsilon_{33} + \left(\frac{1}{4}\langle\epsilon_{33} - \epsilon_{22}\rangle^2 + \frac{1}{2}(\epsilon_{23})^2\right)\left(\frac{\epsilon_{22}^{c0}}{\epsilon_{23}^{s0}}\right)^2 + \epsilon_{13}^2\left(\frac{\epsilon_{22}^{c0}}{\epsilon_{12}^{s0}}\right)^2 + \frac{\eta\langle\sigma_1\rangle}{2}}{(\kappa_2)^2}$$

$$\omega_{2c} = \begin{cases} \bar{\omega}_{2c}, & \text{if } \chi_{2c} \leq \bar{\omega}_{2c} \\ \chi_{2c}, & \text{if } \chi_{2c} > \bar{\omega}_{2c} \end{cases}, \quad \omega_{3c} = \begin{cases} \bar{\omega}_{3c}, & \text{if } \chi_{3c} \leq \bar{\omega}_{3c} \\ \chi_{3c}, & \text{if } \chi_{3c} > \bar{\omega}_{3c} \end{cases}$$

$$(22)$$

(a) Damage evolution in tension   (b) Damage evolution in compression
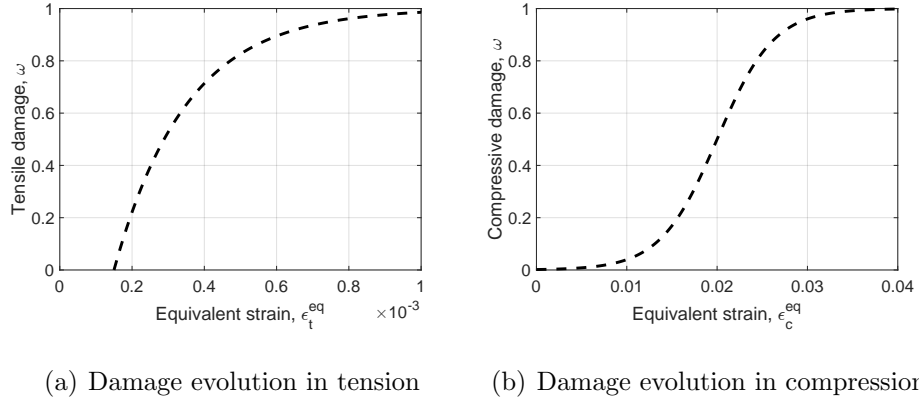
Figure 3: Explicit damage evolution laws.

2.5. Anisotropic nonlocal regularization

The accumulation of damage leads to a softening behavior, which results in localized failure paths in finite element simulations. The energy required to create a unit area of fracture, which should be a material constant, does not

converge upon mesh refinement (Jirásek, 1998). Mathematically, the partial differential equations governing quasi-static problems loose ellipticity, which makes the boundary problem ill-posed. Several regularization techniques exist to avoid mesh dependency and fracture localization, including: the introduction of integration-based variables in the constitutive model (Pijaudier-Cabot and Bažant, 1987; Bažant and Pijaudier-Cabot, 1988; Desmorat et al., 2007; Grassl et al., 2014), gradient-enhanced formulations (De Borst et al., 1995; Peerlings et al., 1996a,b; Geers et al., 1998; Peerlings et al., 1998), the micropolar (Cosserat) continuum theory (Lin et al., 2015; Vernerey et al., 2007), and the local regularization of material properties based on element size and direction (crack band theory) (Hoover and Bažant, 2014; Bažant and Oh, 1983). All of these regularization methods involve an internal length parameter, typically a characteristic length equal to 2 to 3 times the maximum grain size (Bažant and Pijaudier-Cabot, 1989). Note that the gradient theory requires additional boundary conditions, which have no physical meaning, to calculate the third order double stress tensor. The crack band theory fails to capture the process zone of macro fractures. The micropolar continuum theory is particularly suitable for modeling shear bands in granular materials. Here, we adopt a versatile integral-based nonlocal regularization technique, in which the damage evolution and subsequent stiffness reduction at a material point not only depend on the stress state at that point, but also on the stress of points located within a certain neighborhood, the size of which is controlled by internal length parameters. Numerically, we replace the local equivalent strains $\epsilon_{i,k}^{eq}$, used to check damage criteria, by their nonlocal counterparts $\bar{\epsilon}_{i,k}^{eq}$. The nonlocal equivalent strain $\bar{\epsilon}_{i,k}^{eq}$ is caclulated as the weighted

average of the local equivalent strain over an influence volume V, as follows:

$$\bar{\epsilon}_{i,k}^{eq}(\boldsymbol{x}) = \int_V \alpha(\boldsymbol{x}, \boldsymbol{\xi}) \epsilon_{i,k}^{eq}(\boldsymbol{\xi}) \mathbf{d}V(\boldsymbol{\xi}), \quad (i = 1/2, k = t/c). \tag{23}$$

Where $\boldsymbol{x}$ and $\boldsymbol{\xi}$ are the position vectors of the local point considered and of a point located in the influence volume, respectively. $\alpha(\boldsymbol{x}, \boldsymbol{\xi})$ is a weight function, which decreases monotonically when the distance $r = \|\boldsymbol{x} - \boldsymbol{\xi}\|$ increases. In a uniform equivalent strain field $\epsilon^{eq}(\boldsymbol{x})$, the nonlocal strain $\bar{\epsilon}^{eq}(\boldsymbol{x})$ should be uniform and equal to $\epsilon^{eq}(\boldsymbol{x})$. That is why the weight function should also satisfy the following normalizing condition:

$$\int_V \alpha(\boldsymbol{x}, \boldsymbol{\xi}) \mathbf{d}V(\boldsymbol{\xi}) = 1. \tag{24}$$

More generally, we ensure that the partition of unity is satisfied by defining the weight function as follows:

$$\alpha(\boldsymbol{x}, \boldsymbol{\xi}) = \frac{\alpha_0(\boldsymbol{x}, \boldsymbol{\xi})}{V_r(\boldsymbol{x})} = \frac{\alpha_0(\boldsymbol{x}, \boldsymbol{\xi})}{\int_V \alpha_0(\boldsymbol{x}, \boldsymbol{\xi}) \mathbf{d}V(\boldsymbol{\xi})}. \tag{25}$$

Where $V_r(\boldsymbol{x})$ is called the characteristic volume. For isotropic materials, the weight function $\alpha_0(\boldsymbol{x}, \boldsymbol{\xi})$ is often defined as a Gauss function (normal distribution) or a bell-shaped function, with a single internal length. For transversely isotropic materials however, the nonlocal influence zone is direction dependent. Due to the weakening effects of the bedding plane, the development of damage at a point has more influence when cracks propagate in planes that contain the transverse directions than the axial direction (Fig.1). Noting l_{ci} the internal length in direction i, we have: $l_{c3} = l_{c2} > l_{c1}$. Based on these considerations, we propose the following modified bell-shaped

weight function:

$$\alpha_0(\boldsymbol{x}, \boldsymbol{\xi}) = \left\langle 1 - \sum_{i=1}^{3} \frac{\|x_i - \xi_i\|^2}{l_{ci}^2} \right\rangle^2. \tag{26}$$

The internal lengths l_{ci} provide the size of the volume of influence (Fig.4), therefore no cut-off is needed (unlike in the Gauss function).
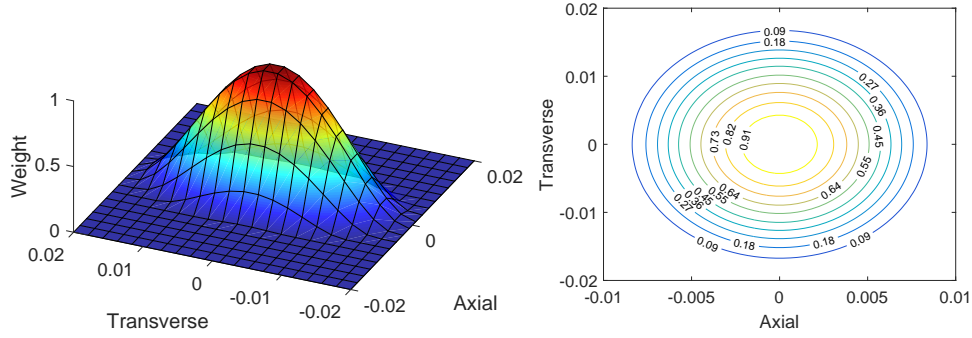

Figure 4: Modified bell-shaped weight function for the nonlocal formulation, with $l_{c1} = 0.01, l_{c2} = 0.02$.

In a Finite Element code, nonlocal averaging and integration are performed by summation over Gauss points located inside the influence zone (De Vree et al., 1995). For instance, the nonlocal equivalent strain is calculated as follows:

$$\bar{\epsilon}_{i,k}^{eq}(\boldsymbol{x}) = \frac{\sum_{j=1}^{N_{GP}} \alpha(\boldsymbol{T}(\boldsymbol{x} - \boldsymbol{\xi}_j)^T)\epsilon_{i,k}^{eq}(\boldsymbol{\xi}_j)\Delta V_j}{\sum_{j=1}^{N_{GP}} \alpha(\boldsymbol{T}(\boldsymbol{x} - \boldsymbol{\xi}_j)^T)\Delta V_j} \tag{27}$$

Where N_{GP} is the total number of Gauss points located within the influence zone. ΔV_j is the integration volume associated with the jth neighboring Gauss point. $\boldsymbol{T}$ is the rotation matrix that transforms global coordinates to local coordinates. In plane strain conditions (adopted in this study), we

19

have:

$$\mathbf{T} = \begin{pmatrix} cos\phi & -sin\phi \\ sin\phi & cos\phi \end{pmatrix} \tag{28}$$

Where ϕ is the counter-clockwise angle between the global and local coordinate systems. In Eq.27, the distance $\|x_i - \xi_i\|$ first introduced in Eq. 26 was replaced by the transformed coordinate components of vector $\boldsymbol{T}(\boldsymbol{x} - \boldsymbol{\xi}_j)^T$.

2.6. Finite Element implementation

Since the damage evolution laws are expressed explicitly, no iteration is needed at the Gauss point to update the state of stress, strain and damage. However, due to the nonlocal formulation adopted here, the calculation of state and internal variables at a point requires calculating the average of the values taken by those variables at the Gauss points located in the influence zone, as explained in Eq.27. In order to handle these calculations, we used an open source package called 'Object Oriented Finite Element Method' (OOFEM) (Patzák and Bittnar, 2004; Patzák, 2012). We used 3D elements without nonlocal regularization and 2D triangular plane strain elements with nonlocal regularization for the following simulations.

At the Gauss point, from the constitutive relations above, the consistent tangent operator (Jacobian matrix) in plane strain can be explicitly derived as follows:

$$\begin{aligned} \mathbf{J} = \frac{\mathrm{d}\boldsymbol{\sigma}}{\mathrm{d}\boldsymbol{\epsilon}} &= \frac{\mathrm{d}\mathbf{C}(\omega_1, \omega_2)}{\mathrm{d}\boldsymbol{\epsilon}} : \boldsymbol{\epsilon} + \mathbf{C}(\omega_1, \omega_2) \\ &= (\frac{\mathrm{d}\mathbf{C}}{\mathrm{d}\omega_1} \frac{\mathrm{d}\omega_1}{\mathrm{d}\kappa_1} \frac{\mathrm{d}\kappa_1}{\mathrm{d}\boldsymbol{\epsilon}} + \frac{\mathrm{d}\mathbf{C}}{\mathrm{d}\omega_2} \frac{\mathrm{d}\omega_2}{\mathrm{d}\kappa_2} \frac{\mathrm{d}\kappa_2}{\mathrm{d}\boldsymbol{\epsilon}}) : \boldsymbol{\epsilon} + \mathbf{C}(\omega_1, \omega_2) \end{aligned} \tag{29}$$

In tension, we have:

$$
\begin{aligned}
\frac{\mathrm{d}\omega_1}{\mathrm{d}\kappa_1} &= \frac{\mathrm{d}\omega_1}{\mathrm{d}\epsilon_{1t}^{eq}} = \frac{\exp(-(\epsilon_{1t}^{eq} - \epsilon_{11}^{t})/\alpha_{11}^{t})}{\alpha_{11}^{t}} \\
\frac{\mathrm{d}\omega_2}{\mathrm{d}\kappa_2} &= \frac{\mathrm{d}\omega_2}{\mathrm{d}\epsilon_{2t}^{eq}} = \frac{\exp(-(\epsilon_{2t}^{eq} - \epsilon_{22}^{t})/\alpha_{22}^{t})}{\alpha_{22}^{t}} \\
\frac{\mathrm{d}\epsilon_{1t}^{eq}}{\mathrm{d}\boldsymbol{\epsilon}} &= \frac{1}{\epsilon_{1t}^{eq}} \left[\begin{array}{cccc} 2\epsilon_{11} & 0 & 0 & 2\epsilon_{12}\left(\frac{\epsilon_{11}^{t}}{\epsilon_{12}^{s}}\right)^2 \end{array} \right]^T \\
\frac{\mathrm{d}\epsilon_{2t}^{eq}}{\mathrm{d}\boldsymbol{\epsilon}} &= \frac{1}{\epsilon_{2t}^{eq}} \left[\begin{array}{cccc} 0 & [2 + \frac{1}{2}\left(\frac{\epsilon_{22}^{t0}}{\epsilon_{23}^{s0}}\right)^2]\epsilon_{22} & 0 & 2\epsilon_{12}\left(\frac{\epsilon_{22}^{t}}{\epsilon_{12}^{s}}\right)^2 \end{array} \right]^T
\end{aligned}
\tag{30}
$$

We obtain the explicit expression of the Jacobian matrix for a compressive stress state in a similar way. The discretization ensures quadratic convergence when solving the global equilibrium equations.

However, with nonlocal enhancement, the Jacobian matrix depends on the state and internal variables of all the Gauss points located within the nonlocal influence zone (Eq.27). Deriving the analytical expression of the tangent operator for a nonlocal formulation is challenging and computationally intensive (Jirásek and Patzák, 2002; Liu et al., 2016; de Pouplana and Oñate, 2016). After assembling all the Finite Element equations, the global stiffness matrix becomes non-symmetric and the half band size increases. In the present case, the proposed nonlocal model considers intrinsic anisotropy, thus matrix rotation is needed whenever the local and global coordinate systems do not coincide. All of these complicated operations make it unfeasible to obtain the nonlocal consistent tangent stiffness matrix analytically. That being said, symmetrical positive definite local secant operators can be used without changing the assembling process. Even if quadratic convergence is lost, the computation terminates successfully (Desmorat et al., 2007; Pegon and Anthoine, 1997).

21

In addition, the degradation of stiffness due to damage induces strain softening, which may result in a global force-displacement curve that exhibits multiple limit points (snap through) and a descending curve (snap-back). A standard load controlled or displacement controlled algorithm based on Newton-Raphson iteration scheme is insufficient to find localized post-peak solutions. In order to overcome this limitation, we adopt an arc length control algorithm. Initially proposed in (Riks, 1979), the essential idea of arc length control is to change the increment of load and the increment of displacement simultaneously. The increments of load and displacement are constrained to ensure that solutions obtained at convergence are indeed on the constitutive stress/strain curve. In this study, we use the so-called spherical arc length method (Crisfield, 1981), in which the constraint equation is expressed as:

$$\mathrm{d}s = \sqrt{\mathrm{d}\boldsymbol{u}^T \mathrm{d}\boldsymbol{u} + \mathrm{d}\lambda^2 \psi^2 \boldsymbol{q}^T \boldsymbol{q}} \tag{31}$$

where $\mathrm{d}s$ is the arc length, $\mathrm{d}\boldsymbol{u}$ is the increment of displacement, $\boldsymbol{q}$ is the external load imposed and λ is a parameter controlling the intensity of the load increment. ψ controls the ratio between the load and displacement increments. Because the constraint equation involves all the degrees of freedom of the domain, it might still encounter convergence issues when localization occurs. Hence, we implement a local version of the arc length control algorithm, based on the local normal plane method (May and Duan, 1997): only the displacement of dominating elements, i.e. elements that contribute to damage growth within the process zone, are used to formulate the constraint equation:

$$\sum_e [\nabla(\mathrm{d}\boldsymbol{u}_1^e)^T \nabla(\mathrm{d}\boldsymbol{u}_i^e)] = (\mathrm{d}s)^2 \quad (i = 1, 2, 3, ...) \tag{32}$$

22

Where e is the element number within the set of dominating elements. Note that the set of dominating elements is only updated at the beginning of each loading increment. For an element with n nodes, $\nabla \boldsymbol{u}$ is the relative displacement vector, defined as follows:

$$\nabla(\boldsymbol{u}^e) = [u_1^e - u_n^e, u_2^e - u_1^e, u_3^e - u_2^e, ..., u_n^e - u_{n-1}^e] \tag{33}$$

3. Calibration and Sensitivity of the Local Damage Model

3.1. Calibration for Bakken shale

The proposed nonlocal anisotropic damage model depends on 5 elastic parameters $(E_1, E_2, \nu_{12}, \nu_{23}, G_{12})$, 13 constitutive parameters that control damage growth under tension and compression $(\epsilon_{11}^{t0}, \alpha_{11}^{t}, \epsilon_{22}^{t0}, \alpha_{22}^{t}, \epsilon_{12}^{s0}, \epsilon_{23}^{s0}, \epsilon_{11}^{c0}, \alpha_{11}^{c}, \beta_{11}^{c}, \epsilon_{22}^{c0}, \alpha_{22}^{c}, \beta_{22}^{c}, \eta)$, and two internal length parameters (l_{c1}, l_{c2}). Except for the fitting parameters α, β and η, all the model parameters have a sound physical meaning. For example, ϵ_{22}^{c0} represents the damage initiation threshold due to compressive strains in the transverse direction. Several stress paths with loading in both axial and transverse directions are required to calibrate all the model parameters, including uniaxial and triaxial compression tests, uniaxial tension tests and directional shear tests. In addition, microstructure images or acoustic measurements are needed to determine the internal lengths. In the following, we calibrate the local damage model against a series of triaxial compression tests performed on North Dakota Bakken shale plugs in ConocoPhillips rock mechanics laboratory (Amendt et al., 2013). Plugs were all cored from the same depth and lithology, both parallel and perpendicular to the bedding plane, and were selected to avoid major bedding

discontinuities. For model calibration, we used the stress/strain curves obtained for a loading perpendicular to the bedding plane under confinements of 1000 psi (6.9 MPa) and 3000 psi (20.7 MPa), and the stress/strain curve obtained for a loading parallel to the bedding plane under a confinement of 3000 psi (20.7 MPa). We validated the model using stress/strain data with loading direction perpendicular to the bedding plane under 2000 psi (13.8 MPa) confinement. The stress paths used for calibration allow determining $E_1, E_2, \nu_{12}, \nu_{23}, \epsilon_{11}^{c0}, \alpha_{11}^c, \beta_{11}^c, \epsilon_{22}^{c0}, \alpha_{22}^c, \beta_{22}^c, \eta$. In the absence of sufficient experimental data, the values of the other parameters $(G_{12}, \epsilon_{11}^{t0}, \alpha_{11}^t, \epsilon_{22}^{t0}, \alpha_{22}^t, \epsilon_{12}^{s0}, \epsilon_{23}^{s0})$ will be assigned values found in the literature for rock materials, as explained below.

We first used a linear regression to obtain the elastic parameters $E_1, E_2,$ ν_{12}, ν_{23}, as shown in Fig.5(e). For all loading directions, only the linear portion of the stress-strain curves were exploited for calibration. Then we used the Interior Point Algorithm in MATLAB to determine the unknown vector $\boldsymbol{B} = (\epsilon_{11}^{c0}, \alpha_{11}^c, \beta_{11}^c, \epsilon_{22}^{c0}, \alpha_{22}^c, \beta_{22}^c, \eta)$ that minimizes the squared residual of the distance between experimental results y_i and numerical predictions $f_i(\boldsymbol{X}, \boldsymbol{B})$. The residual, minimized iteratively, is defined as:

$$R(\boldsymbol{B}) = \sum_{i=1}^{n} [y_i - f_i(\boldsymbol{X}, \boldsymbol{B})]^2 \tag{34}$$

Where $\boldsymbol{X}$ stands for the vector of known input variables of strain. The algorithm was initialized with an initial guess, as well as the lower bound and the upper bound of the coefficients of the unknown parameter vector $\boldsymbol{B}$. Then, triaxial compression tests with different confinement and loading orientations were simulated with the proposed model at the material point, and the value

24

of the residual $R(\boldsymbol{B})$ was calculated based on the set of parameters obtained at the previous iteration. The gradient of the residual $R(\boldsymbol{B})$ with respect to each parameter in the vector $\boldsymbol{B}$ was calculated and used to minimize the difference between numerical and experimental stress-strain curves, as follows:

$$\boldsymbol{B}_{n+1} = \boldsymbol{B}_n - \gamma_n \Delta R(\boldsymbol{B}) \tag{35}$$

Where γ_n is the barrier parameter, which is updated at each iteration step in the Interior Point Algorithm.

Fig.5(a) shows the stress-strain experimental data (markers) and numerical predictions (lines) after calibration with confinements of 6.9 MPa (colored in red) and 20.7 MPa (colored in black), when loading is applied perpendicular to the bedding plane. In addition, we simulated the triaxial compression test with a confinement of 13.8 MPa (blue lines) using the calibrated parameters, and compared the predictions with the experimental data (blue squares). Note that we only used the first portion of the post-peak experimental data, after macroscopic fractures initiate, but before macroscopic fracture propagation becomes dominated by friction along the fracture planes (a propagation regime that cannot be captured by the proposed model). Both lateral and axial stress/strain curves obtained numerically satisfactorily match the experimental data for all confinements, and the proposed model captures the nonlinear hardening and softening behavior and the dependence of strength to confinement. Fig.5(b) shows the evolution of damage for the three tests where loading is perpendicular to the bedding plane. In continuum damage models proposed for materials with no intrinsic anisotropy, transverse damage is produced to reflect the presence of vertical cracks due to devia-

(a) Calibration of the stress-strain curve against triaxial compression tests with axial loading.
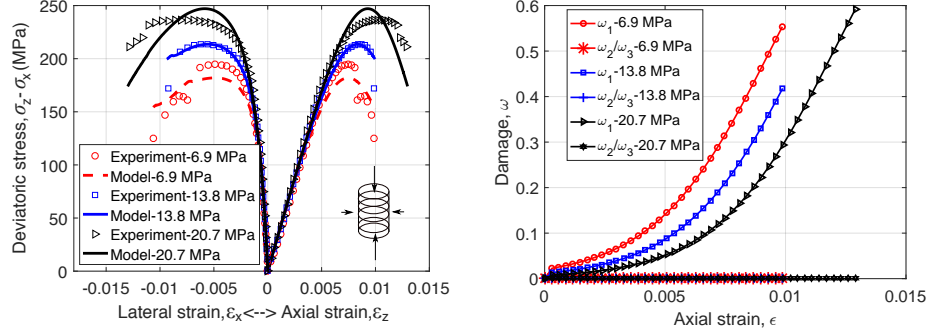
(b) Predicted damage evolution with axial loading (perpendicular to the bedding plane).

(c) Calibration of the stress-strain curve against a triaxial compression test with transverse loading.
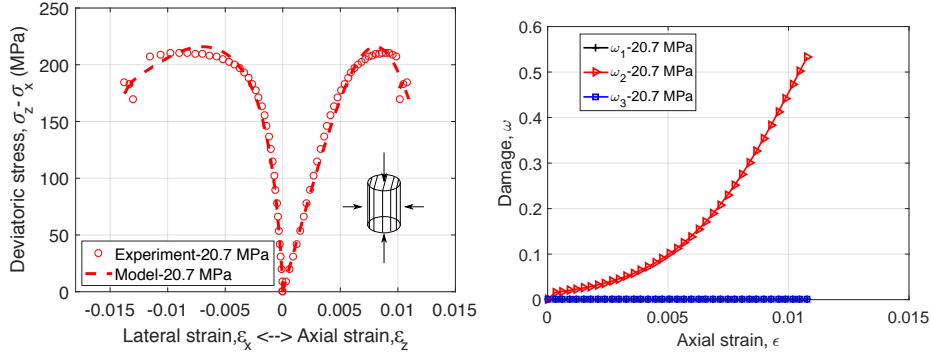
(d) Predicted damage evolution with transverse loading (parallel to the bedding plane).
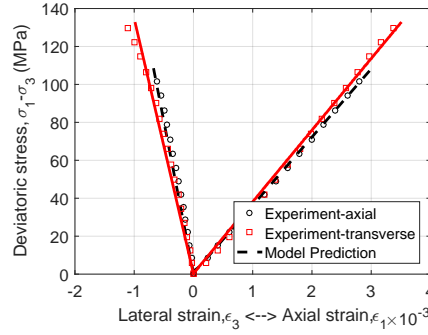
(e) Calibration of the elastic parameters.

26

Figure 5: Calibration of the proposed model against triaxial compression tests performed on Bakken shale for different loading orientations with respect to the bedding plane.

Table 1: Material parameters calibrated from triaxial compression tests.

Direction	Elasticity		Compression			
Axial	E_1/GPa	ν_{12}	ϵ_{11}^{c0}	β_{11}^c	α_{11}^c	η/MPa^{-1}
	3.59	0.22	2.51×10^{-3}	8.02×10^{-3}	2.41×10^{-3}	2.08×10^{-4}
Transverse	E_2/GPa	ν_{23}	ϵ_{22}^{c0}	β_{22}^c	α_{22}^c	η/MPa^{-1}
	3.77	0.33	1.98×10^{-3}	6.39×10^{-3}	2.46×10^{-3}	2.08×10^{-4}

toric stress (Jin et al., 2017; Xu and Arson, 2014; Jin and Arson, 2017c). By contrast, according to the constitutive model in Eq.4, axial damage ω_1 is produced, which results in a reduction of the axial stiffness. When the confining stress is increased, damage initiation occurs at higher axial stress. After damage intiation, the damage rate is independent of the confining pressure.

Fig.5(c) compares the predictions of the calibrated model againts experimental results for a triaxial compression test performed with a loading parallel to the bedding plane, under a 20.7 MPa confinement. Experimental measurements are indicated by circle markers and numerical predictions are represented by dotted lines. For the sake of comparison with the experimental results, we average the two horizontal strain components generated from the model, which are predicted as different due to transverse isotropy, but are not distinguished in the experimental dataset. The experimental and numerical curves match satisfactorily and the proposed model captures the dependence of strength to the loading direction at equal confining pressure (Fig.5(a) and Fig.5(c)). The material parameters calibrated for North Dakota Bakken shale are listed in Table 1.

Table 2: Material parameters assigned with no calibration for the sensitivity analysis.

Direction	Shear	Tension		
Axial	ϵ_{12}^{s0}	ϵ_{11}^{t}	α_{11}^{t}	G_{12}/GPa
	1.8×10^{-4}	1.5×10^{-4}	3.0×10^{-4}	14.68
Transverse	ϵ_{23}^{s0}	ϵ_{22}^{t}	α_{22}^{t}	
	2.6×10^{-4}	2.5×10^{-4}	4.0×10^{-4}	

3.2. Sensitivity analysis of uniaxial tension test

In the absence of datasets on tension and shear tests conducted at various angles compared to the bedding plane, it is impossible to calibrate the remainder of the model parameters ($\epsilon_{11}^{t0}, \alpha_{11}^{t}, \epsilon_{22}^{t0}, \alpha_{22}^{t}, \epsilon_{12}^{s0}, \epsilon_{23}^{s0}, G_{12}$). So we used values that correspond to typical rock properties (Cho et al., 2012) (see Table 2). In order to check that the chosen model parameters are reasonable and to demonstrate that the proposed model can capture the direction dependent stress-strain behavior, we simulated a series of uniaxial tensile tests for various orientation angles θ between the loading axis and the direction normal to the bedding plane (Fig.6(c)). We used a single-cubic-element FEM model with the chosen damage parameters reported in Table 2 and with the calibrated elastic parameters given in Table 1. Displacements at the four bottom nodes were fixed and concentrated forces were applied at the four nodes of the upper face. The arc length control algorithm was used. After the simulations, we extracted the state variables (stress, strain and damage) from the 8 Gauss points and averaged them to generate the plots shown in Fig.6.

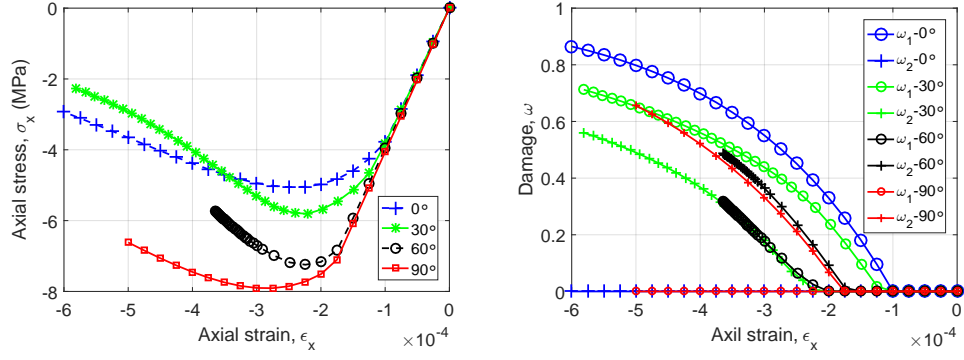Fig.6(a) presents the stress-strain curves of uniaxial tension tests simu-

28

lated with different bedding plane orientations. The elastic part is almost the same in all tests because the Young's moduli E_1, E_2 in the axial and transverse directions are very close (Table 1). However, the maximum stress reached during the test varies with θ: the peak stress is minimum when the loading is applied perpendicular to the bedding plane ($\theta = 0°$), and increases when θ increases. Fig.6(b) shows that, for higher orientation angles θ, the initiation of the axial damage ω_1 occurs under higher axial strain. For $\theta = 90°$, no axial damage is produced (i.e., no cracks along the bedding plane); instead, transverse damage ω_2 is produced (i.e. cracks perpendicular to the bedding plane in non-sliding mode). Fig.6(c) provides the variations of the uniaxial tensile strength (maximum stress reached during loading) with the loading orientation θ. Numerical analyses satisfactorily reproduce published results of indirect Brazilian tests (Cho et al., 2012), both in trend and order of magnitude.

4. Simulation of Anisotropic Fracture Localization

In this section, we solve boundary value problems with the Finite Element Method to test the ability of the model to simulate mesh-independent and direction dependent fracture propagation in mixed mode. We use the constitutive parameters listed in Table 1 and Table 2.

4.1. Three-point bending test

We simulate a three-point bending test. The specimen geometry, notch size and boundary conditions are shown in Fig.7. Linear triangular elements are used in plane strain conditions. The transverse characteristic length l_{c2} is set to 20mm (internal length parallel to the bedding). We study various

(a) Stress-strain curves of simulated uniaxial tension tests.

(b) Evolution of damage during simulated uniaxial tensile tests (components expressed in the local coordinate system of the bedding plane)
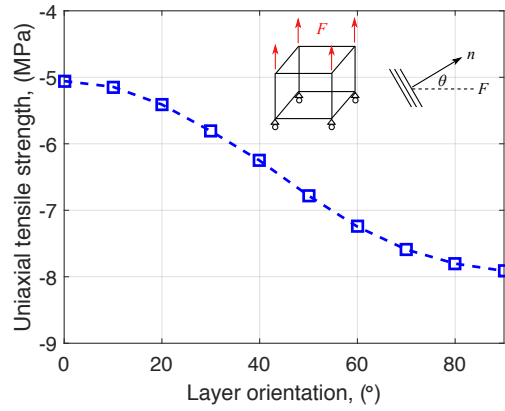
(c) Variation of uniaxial tensile strength (maximum stress reached during the loading) with respect to the angle formed between the loading axis and the direction normal to the bedding plane.

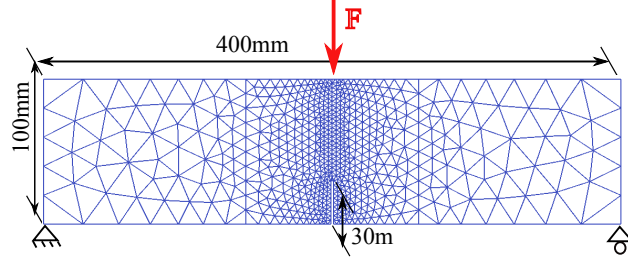Figure 6: Simulation of uniaxial tension tests on a single element. Note: The soil mechanics sign convention is used.

30

Figure 7: Geometry and boundary conditions adopted in the three-point bending test.

ratios $R = l_{c2}/l_{c1}$ to investigate the influence of nonlocal anisotropy on the global response.

Influence of nonlocal enhancement. We first test the nonlocal regularization technique by simulating the three point bending test with and without nonlocal enhancement, for three different mesh densities. In all tests, the loading direction is perpendicular to the bedding plane (orientation noted $\theta = 90°$) and the internal length ratio is set to $R = 2$. Fig.8 shows the post-failure distribution of the transverse damage component ω_2, which corresponds to vertical cracks perpendicular to the bedding plane that propagate by layer breaking (non-sliding mode). Comparing Fig.8(a) and (b), we note that simulations done with the local model exhibit a strong mesh dependency: the width of the fracture process zone is one element in size, no matter what the size of the elements is. As a result, the energy dissipated tends to zero upon mesh refinement. For very fine meshes, no convergence is reached. On the contrary, no mesh dependence is noted with the nonlocal model, as shown in Fig.8(c) and (d). Fig.11(a) shows the variations of the vertical force with vertical displacement at the node where the external load is applied. The peak force and subsequent softening behavior match for all simulations done
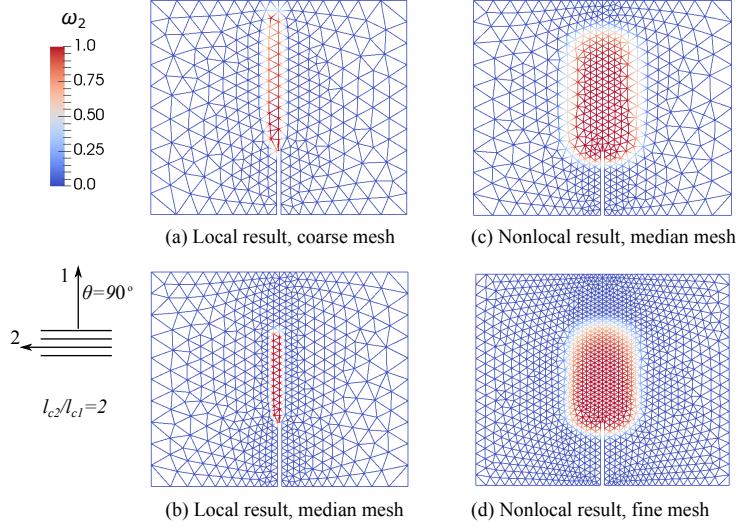
31

Figure 8: Damage distribution in local axis-2 (i.e. vertical cracks perpendicular to the bedding plane) obtained in the three-point bending tests, without and with nonlocal enhancement, for various mesh densities. In all cases, bedding orientation angle is $\theta = 90°$, and the internal length ratio is $l_{c2}/l_{c1} = 2$.

with the nonlocal model, whereas they differ in the simulations done with the local model. Results thus confirm that the regularization technique not only alleviates mesh dependency for the failure path, but also for the global response of the domain. Note that in this particular test, nonlocal enhancement results in an increased stiffness of the domain, which turns out to be 2-3 times larger than that obtained with the local model. This points out the importance of proper calibration of the internal length parameters.

Influence of the bedding orientation (intrinsic anisotropy). Now that we showed that the nonlocal model alleviates mesh dependency, we perform all the simulations with the median-sized mesh. Fig.9 shows the damage process zone for different bedding orientations, and highlights the underlying failure mecha-

nism. When the loading force is parallel to the bedding plane ($\theta = 0°$), only axial damage (ω_1) develops, wich corresponds to weak plane debonding. Damage propagates in pure mode I right above the notch. In the case of $\theta = 30°$, failure in mixed mode is observed. Damage propagates in both the axial (ω_1) and transverse (ω_2) directions of the bedding coordinate system. The failure path initially follows the bedding direction, and then turns up to be parallel to the loading force direction. The extent of the damage zone is larger for ω_1 than ω_2. Similarly, when the bedding orientation angle is $60°$ with respect to the horizontal axis, damage propagates in mixed mode in both axial and transverse directions (ω_1, ω_2). The adopted resolution algorithm still has some shortcomings when the global response exhibits severe snap back behavior: convergence issues still exist and it is impossible to obtain the final expected damage zone. Here, we show the intermediate damage process zone, obtained just before the calculation stopped: at this stage, damage propagates mostly along the bedding plane; alignment with the loading force has just started. When the bedding plane is horizontal ($\theta = 90°$), the damage zone aligns with the notch like in the case of a vertical bedding plane ($\theta = 0°$), but failure is mostly due to layer breakage and not weak plane debonding: $\omega_2 > \omega_1$. As expected, the overall size of the damage process zone increases as the angle θ between the loading direction and the transverse bedding plane direction increases. Fig.11(b) shows the load-deflection curves obtained at the node where the external force is applied, for the four cases simulated. The maximum load force required to induce failure increases as the bedding orientation angle θ increases. This could be expected: weak plane debonding at $\theta = 0°$ requires less energy than
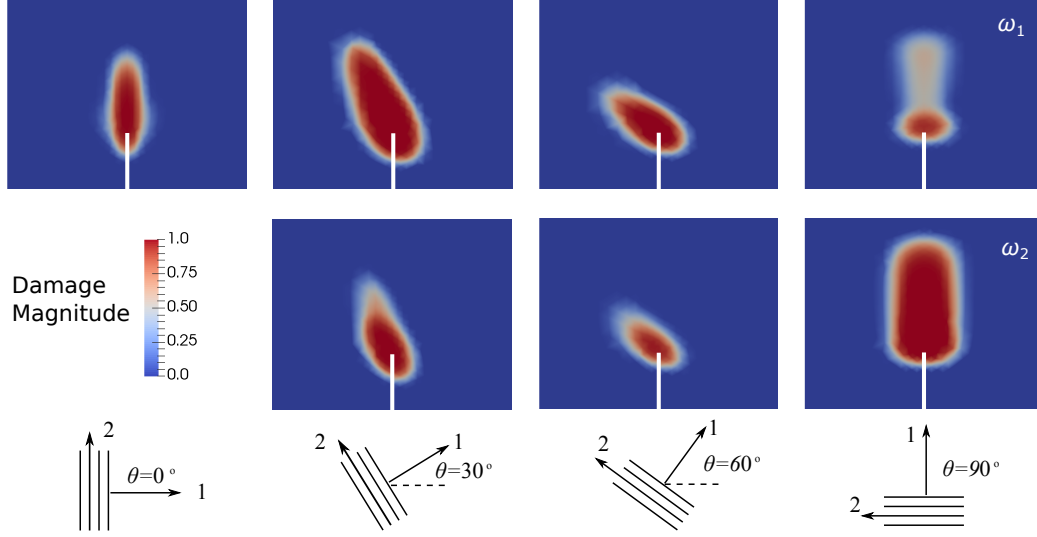
33

Figure 9: Spatial distribution of the tensile damage components expressed in the local coordinate system of the bedding plane, for loads applied at an angle $\theta = 0°, 30°, 60°, 90°$ compared to the transverse direction of the bedding plane.

layer breakage at $\theta = 90°$. Note that the local arc length control method employed in the resolution algorithm makes it possible to predict the snap back behavior (decreasing load with decreasing displacement) in the case of $\theta \neq 90°$.

Influence of the ratio of internal lengths (microstructure). We analyze the influence of the internal length ratio $R = l_{c2}/l_{c1}$ for $l_{c2} = 20$ mm (Fig.10). We use the median sized mesh and we study two bedding orientations: $\theta = 0°, 90°$. Damage propagates in mode I due to weak layer debonding in the case of $\theta = 0°$, and due to layer breakage in the case of $\theta = 90°$. Since the extent of the influence zone in the transverse direction is the same in all simulations (i.e., l_{c2} is fixed), the width of the transverse damage process zone is the same

for all simulations with $\theta = 90°$. By contrast, the length of the transverse damage zone inccreases with l_{c1}. Similarly, for $\theta = 0°$, the area of the axial damage zone increases with l_{c1} (i.e. increases when $R = l_{c2}/l_{c1}$ decreases). Microstructure anisotropy, represented by the internal length parameters, thus translates into anisotropy of the damage process zone. When comparing the load-displacement curves (Fig.11), we note that for both $\theta = 0°$ and $90°$, a higher peak force is reached for a lower internal length ratio R (i.e. for an increasing internal length l_{c1}). A lower force is required to cause failure by weak plane debonding when the axial internal length l_{c1} is high. For $\theta = 0°$, we note that the post-peak portion of the load-displacement curves match. We hypothesize that the internal length l_{c2}, fixed to the same value in all the simulations, controls the post-peak softening behavior. The exceptionally high value of the peak force for $R = 1$, $\theta = 0°$ can be explained by the large size of the influence zone in that particular case, delimited by the circles in Fig.10.

4.2. Splitting test

We simulate splitting tests described in Comi and Perego (2001) to investigate compressive damage development for various bedding orientations. The geometry and boundary conditions are shown in Fig.12. Plane strain triangular elements are used to mesh the domain. Since the nonlocal formulation proved to successfully alleviate mesh dependency in the previous case studies, we only use one mesh density for the splitting test simulations. The transverse characteristic length l_{c2} is set to 20mm; the axial internal length l_{c1} is set to 10mm. We simulate a force-controlled test, which allows using the local arc length control method to solve the global FEM equations by
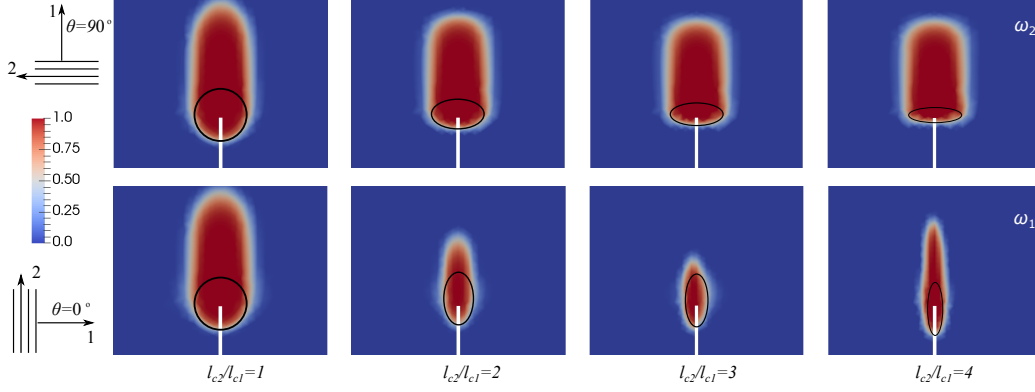
Figure 10: Spatial distribution of the tensile damage component in the transverse direction 2 (cracks perpendicular to the bedding plane) for orientation angle $\theta = 90°$, and in the axial direction 1 (cracks parallel to the bedding plane) for orientation angle $\theta = 0°$, for various internal length ratios defined as $R = l_{c2}/l_{c1}$.

scaling load and displacement increments at each iteration. A uniform stress is applied on the top central part of the sample, and we stop the simulation once the applied stress reaches 100 MPa (Fig.12).

Fig.13 shows the spatial distribution of damage for various bedding orientations, and also indicates the potential failure path at macro scale. For $\theta = 0°$ (vertical bedding plane, parallel to the loading direction), the failure mechanism is dominated by the propagation of horizontal cracks, i.e. transverse compression damage ω_{2c}. This is counter-intuitive: the failure mechanism was expected to be controlled by weak plane debonding resulting in verical planes. This discrepancy comes from the construction of the model itself, in which compressive equivalent strains are used to calculate compressive damage in axial and transverse directions, which are directly injected in the expression of the stiffness tensor to account for the degradation of elastic

36
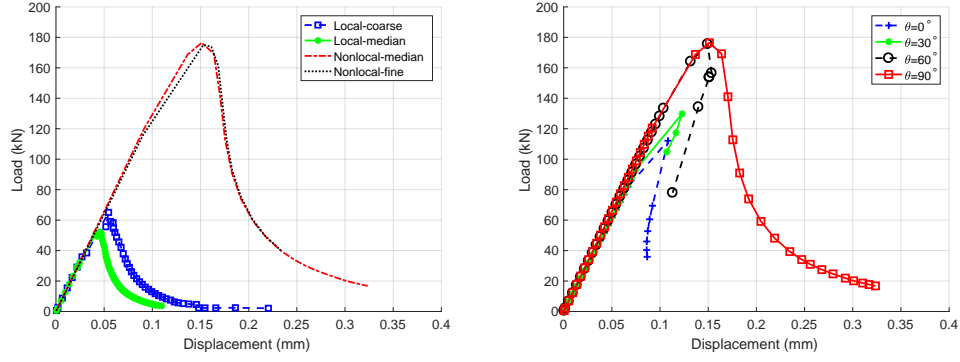
(a) Force-displacement curves with and without nonlocal enhancement.

(b) Force-displacement curves for various bedding orientations.
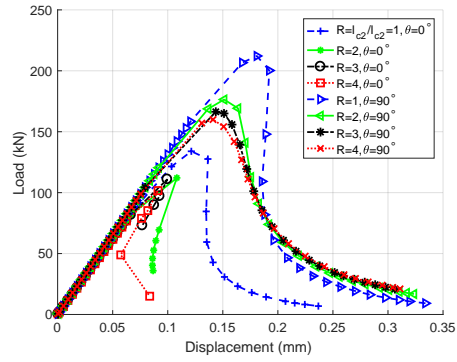
(c) Force-displacement curves for various internal length ratios.

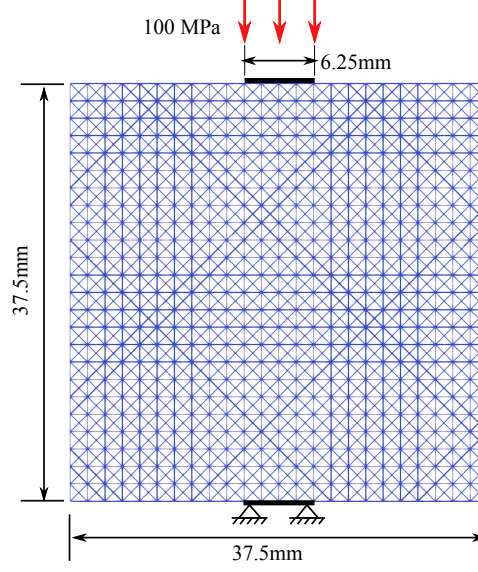Figure 11: Force-displacement curves at the node where the load is applied during the three-point bending tests.

Figure 12: Geometry, mesh and boundary conditions of the splitting test, simulated based on experiments reported in (Comi and Perego, 2001).

properties. Similarly for $\theta = 90°$ (horizontal bedding plane, perpendicular to the loading direction), the main failure mechanism is the development of horizontal cracks, i.e. axial compressive damage ω_{1c}. However, both of these two cases yield vertical fracture paths (damage concentration zone) along the central line at sample scale, which is conform to experimental observations (Comi and Perego, 2001). For $\theta = 30°$ and $\theta = 60°$, the proposed model does not only capture the macro failure paths (the fracture propagates through the sample at an angle with respect to the loading direction), but also reveals the underlying failure mechanism. The compressive shear damage ω_{2c} controls the failure for the case of $\theta = 30°$, and the compressive sliding along the layers ω_{1c} is the dominating failure mechanism for $\theta = 60°$. It is clear that the development of damage and the formation of fracture paths are direction
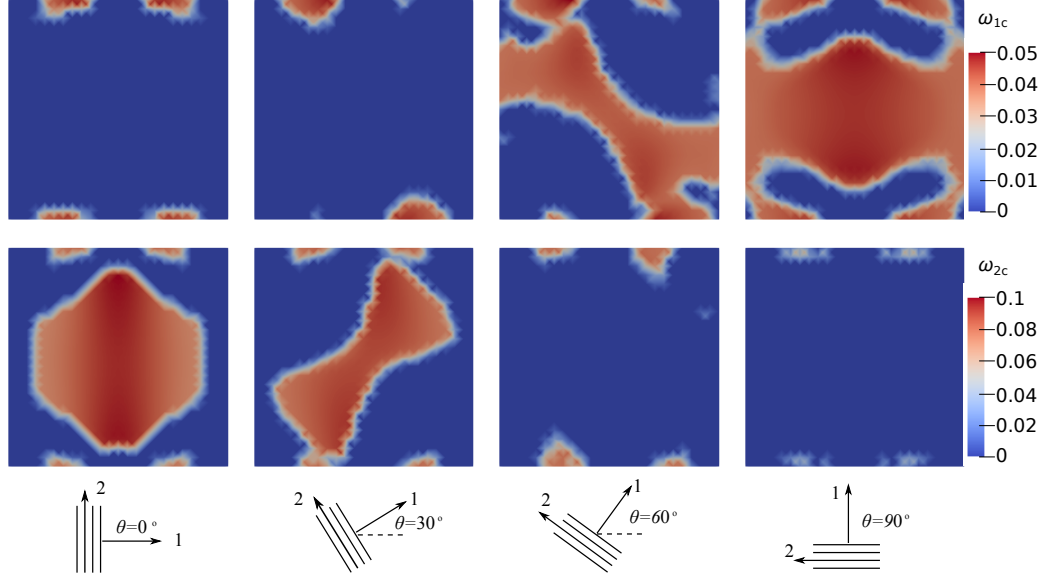
38

Figure 13: Spatial distribution of the tensile and compressive damage components in the axial and transverse directions, with a bedding plane of various orientations.

dependent.

5. Conclusions

The proposed model is designed to predict the complex non-linear behavior of materials with intrinsic anisotropy upon crack propagation. Crack initiation and propagation are modeled by phenomenological damage evolution laws. The principle of equivalent elastic deformation is used to calculate the stiffness tensor of the damaged material. Following the choice of stress invariants made in Hill's quadratic yield criteria (for orthotropic materials) and Hashin's failure criteria (for unidirectional fiber composites), four equivalent strain measures are constructed to distinguish the mechanical response

of the material in tension and compression, along the direction perpendicular to the bedding plane and within the bedding plane. Damage evolution laws are formulated explicitly in terms of the maximum equivalent strain ever encountered in the loading history. For Finite Element implementation, the equivalent strains are replaced by nonlocal counterparts, defined as weighted averages over a certain neighborhood, the size of which is controlled by two internal length parameters that represent microstructure anisotropy. Due to the complexities involved in the derivation of the tangent operator with nonlocal models, we used a local secant operator and solved the Finite Element equations with a normal plane arc length control algorithm, which allows passing limit points in case of snap back or snap through.

Model calibration requires knowing the material behavior for several bedding plane orientations under several independent stress paths. Elastic and compression damage parameters were calibrated against triaxial compression test data of Bakken shale with axial loading parallel and perpendicular to the bedding under different confinements. Sensitivity analyzes confirmed that the model successfully captures the variation of uniaxial tensile strength with respect to the bedding orientation. Finite Element simulations of three-point bending tests and compression splitting tests showed that nonlocal enhancement indeed avoids mesh dependency and that the size of the damage process zone along and perpendicular to the bedding plane is scaled by the two characteristic lengths. Results further show that the damage process zone is direction dependent both in tension and compression. In particular, the three-point bending test simulations reveal that mixed mode fracture propagation dominates when the loading force is not aligned with the bed-

ding plane.

Although calibrated for geomaterials, the proposed damage model with anisotropic nonlocal enhancement can be applied to any brittle textured material, such as ceramics, polymers or metals. Anisotropy is accounted for at the microstructure scale and at the phenomenological scale of the REV. Damage constitutive laws are direction-specific, which makes it possible to represent several concurrent damage mechanisms in the macroscopic response, and to interpret the failure mechanisms that control the damage process zone. Hence, the proposed modeling approach and the associated numerical methods employed in this paper can be utilized to solve a wide range of engineering problems involving the mechanical integrity of structural members, borehole stability, or delamination of composites, to cite only a few. Future work will be dedicated to calibration methods and microstructure-enrichment for a more precise and computationally effective topological representation of the damage process zone.

Acknowledgements

41

References

Amendt, D., Busetti, S., Wenning, Q., et al., 2013. Mechanical characterization in unconventional reservoirs: A facies-based methodology. Petrophysics 54 (05), 457–464.

Bažant, Z. P., Oh, B. H., 1983. Crack band theory for fracture of concrete. Materials and structures 16 (3), 155–177.

Bažant, Z. P., Pijaudier-Cabot, G., 1988. Nonlocal continuum damage, localization instability and convergence. Journal of Applied Mechanics 55 (2), 287–293.

Bažant, Z. P., Pijaudier-Cabot, G., 1989. Measurement of characteristic length of nonlocal continuum. Journal of Engineering Mechanics 115 (4), 755–767.

Boehler, J., Sawczuk, A., 1977. On yielding of oriented solids. Acta Mechanica 27 (1-4), 185–204.

Bramlette, M. N., 1943. US Geological Survey Professional Paper. No. 212. US Government Printing Office.

Cazacu, O., Cristescu, N., 1999. A paraboloid failure surface for transversely isotropic materials. Mechanics of materials 31 (6), 381–393.

Cazacu, O., Cristescu, N., Shao, J., Henry, J., 1998. A new anisotropic failure criterion for transversely isotropic solids. Mechanics of Cohesive-frictional Materials 3 (1), 89–103.

Chen, L., Shao, J., Zhu, Q., Duveau, G., 2012. Induced anisotropic damage and plasticity in initially anisotropic sedimentary rocks. International Journal of Rock Mechanics and Mining Sciences 51, 13–23.

Chen, L., Shao, J.-F., Huang, H., 2010. Coupled elastoplastic damage modeling of anisotropic rocks. Computers and Geotechnics 37 (1), 187–194.

Cho, J.-W., Kim, H., Jeon, S., Min, K.-B., 2012. Deformation and strength anisotropy of asan gneiss, boryeong shale, and yeoncheon schist. International Journal of Rock Mechanics and Mining Sciences 50, 158–169.

Comi, C., Perego, U., 2001. Fracture energy based bi-dissipative damage model for concrete. International Journal of Solids and Structures 38 (36), 6427–6454.

Comi, C., Perego, U., 2004. Criteria for mesh refinement in nonlocal damage finite element analyses. European Journal of Mechanics-A/Solids 23 (4), 615–632.

Crisfield, M. A., 1981. A fast incremental/iterative solution procedure that handles "snap-through". Computers & Structures 13 (1), 55–62.

Dafalias, Y. F., Papadimitriou, A. G., Li, X. S., 2004. Sand plasticity model accounting for inherent fabric anisotropy. Journal of Engineering Mechanics 130 (11), 1319–1333.

De Borst, R., Pamin, J., Peerlings, R., Sluys, L., 1995. On gradient-enhanced damage and plasticity models for failure in quasi-brittle and frictional materials. Computational Mechanics 17 (1-2), 130–141.

de Pouplana, I., Oñate, E., 2016. Combination of a non-local damage model for quasi-brittle materials with a mesh-adaptive finite element technique. Finite Elements in Analysis and Design 112, 26–39.

De Vree, J., Brekelmans, W., Van Gils, M., 1995. Comparison of nonlocal approaches in continuum damage mechanics. Computers & Structures 55 (4), 581–588.

Desmorat, R., Gatuingt, F., Ragueneau, F., 2007. Nonlocal anisotropic damage model and related computational aspects for quasi-brittle materials. Engineering Fracture Mechanics 74 (10), 1539–1560.

Donath, F. A., 1961. Experimental study of shear failure in anisotropic rocks. Geological Society of America Bulletin 72 (6), 985–989.

Fu, Y., Iwata, M., Ding, W., Zhang, F., Yashima, A., 2012. An elastoplastic model for soft sedimentary rock considering inherent anisotropy and confining-stress dependency. Soils and Foundations 52 (4), 575–589.

Gallant, C., Zhang, J., Wolfe, C. A., Freeman, J., Al-Bazali, T. M., Reese, M., et al., 2007. Wellbore stability considerations for drilling high-angle wells through finely laminated shale: a case study from terra nova. In: SPE Annual Technical Conference and Exhibition. Society of Petroleum Engineers.

Gautam, R., Wong, R. C., 2006. Transversely isotropic stiffness parameters and their measurement in colorado shale. Canadian Geotechnical Journal 43 (12), 1290–1305.

Geers, M., De Borst, R., Brekelmans, W., Peerlings, R., 1998. Strain-based transient-gradient damage model for failure analyses. Computer Methods in Applied Mechanics and Engineering 160 (1), 133–153.

Grassl, P., Xenos, D., Jirásek, M., Horák, M., 2014. Evaluation of nonlocal approaches for modelling fracture near nonconvex boundaries. International Journal of Solids and Structures 51 (18), 3239–3251.

Halm, D., Dragon, A., Charles, Y., 2002. A modular damage model for quasi-brittle solids–interaction between initial and induced anisotropy. Archive of Applied Mechanics 72 (6-7), 498–510.

Hashagen, F., De Borst, R., 2001. Enhancement of the hoffman yield criterion with an anisotropic hardening model. Computers & Structures 79 (6), 637–651.

Hashin, Z., 1980. Failure criteria for unidirectional fiber composites. Journal of applied mechanics 47 (2), 329–334.

Heng, S., Guo, Y., Yang, C., Daemen, J. J., Li, Z., 2015. Experimental and theoretical study of the anisotropic properties of shale. International Journal of Rock Mechanics and Mining Sciences 74, 58–68.

Hill, R., 1948. A theory of the yielding and plastic flow of anisotropic metals. In: Proceedings of the Royal Society of London A: Mathematical, Physical and Engineering Sciences. Vol. 193. The Royal Society, pp. 281–297.

Hoffman, O., 1967. The brittle strength of orthotropic materials. Journal of Composite Materials 1 (2), 200–206.

Hoover, C. G., Bažant, Z. P., 2014. Cohesive crack, size effect, crack band and work-of-fracture models compared to comprehensive concrete fracture tests. International Journal of Fracture 187 (1), 133–143.

Hu, D., Zhou, H., Zhang, F., Shao, J., Zhang, J., 2013. Modeling of inherent anisotropic behavior of partially saturated clayey rocks. Computers and Geotechnics 48, 29–40.

Huerta, A., Pijaudier-Cabot, G., 1994. Discretization influence on regularization by two localization limiters. Journal of engineering mechanics 120 (6), 1198–1218.

Jin, W., Arson, C., 2017a. Discrete equivalent wing crack based damage model for brittle solids. International Journal of Solids and Structures 110-111, 279–293.

Jin, W., Arson, C., 2017b. Micromechanics based discrete damage model with multiple non-smooth yield surfaces: theoretical formulation, numerical implementation and engineering applications. International Journal of Damage Mechanics, 1056789517695872.

Jin, W., Arson, C., 2017c. Modeling of tensile and compressive damage in layered sedimentary rock: A direction dependent non-local model. In: 51st US Rock Mechanics/Geomechanics Symposium. American Rock Mechanics Association.

Jin, W., Xu, H., Arson, C., Busetti, S., 2017. Computational model coupling mode ii discrete fracture propagation with continuum damage zone

evolution. International Journal for Numerical and Analytical Methods in Geomechanics 41, 223–250.

Jirásek, M., 1998. Nonlocal models for damage and fracture: comparison of approaches. International Journal of Solids and Structures 35 (31), 4133–4145.

Jirásek, M., Patzák, B., 2002. Consistent tangent stiffness for nonlocal damage models. Computers & structures 80 (14), 1279–1293.

Li, C., Caner, F. C., Chau, V. T., Bažant, Z. P., 2017. Spherocylindrical microplane constitutive model for shale and other anisotropic rocks. Journal of the Mechanics and Physics of Solids 103, 155–178.

Lin, J., Wu, W., Borja, R. I., 2015. Micropolar hypoplasticity for persistent shear band in heterogeneous granular materials. Computer Methods in Applied Mechanics and Engineering 289, 24–43.

Liu, P., Gu, Z., Yang, Y., Peng, X., 2016. A nonlocal finite element model for progressive failure analysis of composite laminates. Composites Part B: Engineering 86, 178–196.

May, I., Duan, Y., 1997. A local arc-length procedure for strain softening. Computers & structures 64 (1), 297–303.

Mazars, J., 1986. A description of micro- and macroscale damage of concrete structures. Engineering Fracture Mechanics 25 (5), 729–737.

Mazars, J., Pijaudier-Cabot, G., 1989. Continuum damage theory-

application to concrete. Journal of Engineering Mechanics 115 (2), 345–365.

Nasseri, M., Rao, K., Ramamurthy, T., 2003. Anisotropic strength and deformational behavior of himalayan schists. International Journal of Rock Mechanics and Mining Sciences 40 (1), 3–23.

Nedjar, B., 2016. On a concept of directional damage gradient in transversely isotropic materials. International Journal of Solids and Structures 88, 56–67.

Niandou, H., Shao, J., Henry, J., Fourmaintraux, D., 1997. Laboratory investigation of the mechanical behaviour of tournemire shale. International Journal of Rock Mechanics and Mining Sciences 34 (1), 3–16.

Oda, M., Nakayama, H., 1989. Yield function for soil with anisotropic fabric. Journal of Engineering Mechanics 115 (1), 89–104.

OKA, F., KIMOTO, S., KOBAYASHI, H., ADACHI, T., 2002. Anisotropic behavior of soft sedimentary rock and a constitutive model. Soils and foundations 42 (5), 59–70.

Patzák, B., 2012. Oofem—an object-oriented simulation tool for advanced modeling of materials and structures. Acta Polytechnica 52 (6).

Patzák, B., Bittnar, Z., 2004. Oofem–an object oriented framework for finite element analysis. Acta Polytechnica 44 (5-6).

Peerlings, R., De Borst, R., Brekelmans, W., De Vree, J., Spee, I., 1996a.

Some observations on localisation in non-local and gradient damage models. European Journal of Mechanics - A/Solids 15, 937–954.

Peerlings, R., De Borst, R., Brekelmans, W., Geers, M., 1998. Gradient-enhanced damage modelling of concrete fracture. Mechanics of Cohesive-frictional Materials 3 (4), 323–342.

Peerlings, R., De Borst, R., De Vree, J., 1996b. Gradient enhanced damage for quasi-brittle materials. International Journal for numerical methods in engineering 39 (De Vree, JHP), 3391–3403.

Pegon, P., Anthoine, A., 1997. Numerical strategies for solving continuum damage problems with softening: application to the homogenization of masonry. Computers & structures 64 (1), 623–642.

Pietruszczak, S., Lydzba, D., Shao, J.-F., 2002. Modelling of inherent anisotropy in sedimentary rocks. International Journal of Solids and Structures 39 (3), 637–648.

Pietruszczak, S., Mroz, Z., 2000. Formulation of anisotropic failure criteria incorporating a microstructure tensor. Computers and Geotechnics 26 (2), 105–112.

Pietruszczak, S., Mroz, Z., 2001. On failure criteria for anisotropic cohesive-frictional materials. International Journal for Numerical and Analytical Methods in Geomechanics 25 (5), 509–524.

Pijaudier-Cabot, G., Bažant, Z. P., 1987. Nonlocal damage theory. Journal of Engineering Mechanics 113 (10), 1512–1533.

Reinicke, K., Ralston, T., 1977. Plastic limit analysis with an anisotropic, parabolic yield function. In: International Journal of Rock Mechanics and Mining Sciences & Geomechanics Abstracts. Vol. 14. Elsevier, pp. 147–162.

Riks, E., 1979. An incremental approach to the solution of snapping and buckling problems. International Journal of Solids and Structures 15 (7), 529–551.

Rouabhi, A., Tijani, M., Rejeb, A., 2007. Triaxial behaviour of transversely isotropic materials: application to sedimentary rocks. International Journal for Numerical and Analytical Methods in Geomechanics 31 (13), 1517–1535.

Schellekens, J., De Borst, R., 1990. The use of the hoffman yield criterion in finite element analysis of anisotropic composites. Computers & Structures 37 (6), 1087–1096.

Sone, H., Zoback, M. D., 2013. Mechanical properties of shale-gas reservoir rocks—part 1: Static and dynamic elastic properties and anisotropy. Geophysics 78 (5), D381–D392.

Tien, Y. M., Kuo, M. C., 2001. A failure criterion for transversely isotropic rocks. International Journal of Rock Mechanics and Mining Sciences 38 (3), 399–412.

Tsai, S. W., Wu, E. M., 1971. A general theory of strength for anisotropic materials. Journal of composite materials 5 (1), 58–80.

Vernerey, F., Liu, W. K., Moran, B., 2007. Multi-scale micromorphic theory for hierarchical materials. Journal of the Mechanics and Physics of Solids 55 (12), 2603–2651.

Vervoort, A., Min, K.-B., Konietzky, H., Cho, J.-W., Debecker, B., Dinh, Q.-D., Frühwirt, T., Tavallali, A., 2014. Failure of transversely isotropic rock under brazilian test conditions. International Journal of Rock Mechanics and Mining Sciences 70, 343–352.

Waters, G. A., Lewis, R. E., Bentley, D., et al., 2011. The effect of mechanical properties anisotropy in the generation of hydraulic fractures in organic shales. In: SPE Annual Technical Conference and Exhibition. Society of Petroleum Engineers.

Xu, H., Arson, C., 2014. Anisotropic damage models for geomaterials: theoretical and numerical challenges. International Journal of Computational Methods 11 (02), 1342007.

Ye, Z., Ghassemi, A., 2016. Deformation properties of saw-cut fractures in barnett, mancos and pierre shales. In: 50th US Rock Mechanics/Geomechanics Symposium, Houston, Texas, USA.

Ye, Z., Ghassemi, A., Riley, S., 2016. Fracture properties characterization of shale rocks. In: Unconventional Resources Technology Conference, San Antonio, Texas, 1-3 August 2016. Society of Exploration Geophysicists, American Association of Petroleum Geologists, Society of Petroleum Engineers, pp. 1083–1095.